Aerosol Science and Technology
Publication details, including instructions for authors and subscription information:
http://www.informaworld.com/smpp/title~content=t713656376

Image Analysis and Computer Simulation of Nanoparticle Clustering in Combustion Systems

Y. H. Chen [a]; S. D. Bakrania [a]; M. S. Wooldridge [ab]; A. M. Sastry [acd]
[a] Department of Mechanical Engineering, University of Michigan, Ann Arbor, Michigan, USA [b] Department of Aerospace Engineering, University of Michigan, Ann Arbor, Michigan, USA [c] Department of Biomedical Engineering, University of Michigan, Ann Arbor, Michigan, USA [d] Department of Materials Science and Engineering, University of Michigan, Ann Arbor, Michigan, USA

First published on: 10 December 2009

To cite this Article Chen, Y. H., Bakrania, S. D., Wooldridge, M. S. and Sastry, A. M.(2010) 'Image Analysis and Computer Simulation of Nanoparticle Clustering in Combustion Systems', Aerosol Science and Technology, 44: 1, 83 — 95, First published on: 10 December 2009 (iFirst)
To link to this Article: DOI: 10.1080/02786820903390380
URL: http://dx.doi.org/10.1080/02786820903390380

Aerosol Science and Technology, 44:83–95, 2010

ISSN: 0278-6826 print / 1521-7388 online
DOI: 10.1080/02786820903390380

Image Analysis and Computer Simulation of Nanoparticle Clustering in Combustion Systems

Y.-H. Chen,[1] S. D. Bakrania,[1] M. S. Wooldridge,[1,2] and A. M. Sastry[1,3,4]

[1]*Department of Mechanical Engineering, University of Michigan, Ann Arbor, Michigan, USA*
[2]*Department of Aerospace Engineering, University of Michigan, Ann Arbor, Michigan, USA*
[3]*Department of Biomedical Engineering, University of Michigan, Ann Arbor, Michigan, USA*
[4]*Department of Materials Science and Engineering, University of Michigan, Ann Arbor, Michigan, USA*

The current work presents a new method to model and characterize the formation and growth of nanoparticles clusters which includes the three dimensional geometric properties of the clusters, such as aspect ratios, main chain length, radius of gyration, fractal dimension and fractal prefactor. In the model, semi-stochastic mathematics is used to represent varying levels of Coulomb and van der Waals forces during clustering of monodisperse particles. Parametric studies of the relative particle interactions are conducted to evaluate the effects on cluster geometry. Radius of gyration and main chain length were identified as the geometric properties with the greatest sensitivity to changes in the interparticle forces. To demonstrate the analytical capability of the approach, clusters of combustion-generated tin dioxide (SnO_2) nanoparticles were imaged and evaluated to identify the dominant forces controlling cluster morphology. The results show the geometry of the SnO_2 clusters is a result of strong Coulomb interactions.

[Supplementary materials are available for this article. Go to the publisher's online edition of *Aerosol Science and Technology* to view the free supplementary files.]

1. INTRODUCTION

Megatons of particulates are produced annually by combustion methods including desirable nanomaterials (Pratsinis 1998; Wooldridge 1998; Nowack and Bucheli 2007) and toxic byproducts (Nizich et al. 2000). These wide-ranging applications have motivated considerable efforts to develop predictive capabilities for particulate properties such as particulate number density, composition, size, and morphology. A broad range of approaches is documented in the literature; however, modeling particulate formation and growth with any reasonable degree of accuracy remains a significant challenge.

Recieved 17 June 2009; accepted 2 October 2009.
Address correspondence to Ann Marie Sastry, Department of Mechanical Engineering, University of Michigan, 2350 Hayward Street, Ann Arbor, Michigan 48109-2125, USA. E-mail: amsastry@umich.edu

Most particulate formation and growth models focus on limited size regimes, and rarely do modeling approaches attempt to span the orders of magnitude associated with the growth of incipient particles, consisting of clusters of atoms, to the formation of nano- and micron-scale particulates with complex 3-dimensional structures. Relevant chemical and physical processes include nucleation, agglomeration (formation of soft bonds), aggregation (formation of hard bonds), surface growth (heterogeneous reaction and condensation), fragmentation, restructuring (sintering or coalescence), and oxidation. Indeed, the challenges of spanning such dimensions and diverse processes are considerable.

In general, particle nucleation, surface growth, agglomeration, and coalescence can be considered various modes of particle clustering, where the particles involved in collisions can range from single atoms to nano-aggregates. This work explores the use of particle-clustering statistics as a means to simulate the particle formation and growth processes. Towards this goal, the current work presents the development and demonstration of a semi-stochastic method for predicting particulate morphology and for analysis of the forces important during interparticle collision. A combustion nanoparticle synthesis system is the test bed for the study.

2. SCIENTIFIC BACKGROUND

2.1. Particle Formation and Growth Models

Because high-temperature gas-phase combustion systems that produce ceramic, metal and carbonaceous nanoparticles are generally not well described by classical nucleation theory (Wu et al. 1987; Zachariah and Semerjian 1989; Xiong and Pratsinis 1991), theoretical modeling for these systems is invariably based on collision kinetics. The modeling approach and theory invoked are determined based on the size of the particles under consideration. For example, the early growth process (forming clusters of <10 atoms or molecules) has been modeled as polymerization of monomers using approximations and theory indicated by comparison with gas-phase reactions, e.g.,

TABLE 1
Methods used to validate and/or represent interactions between nanoparticle collisions

Nanoparticle system	Process used to create nanoparticles	Force identified (experimental)/ force applied (simulation)	Validation method	Reference
Si	silane pyrolysis	Coulomb	experimental	Onischuk et al. (2000)
carbonaceous soot	propane combustion	Coulomb	experimental	Onischuk et al. (2000)
TiO_2	flame synthesis of $TiCl_4$	van der Waals	experimental	Froeschke et al. (2003)
Ag, Ni	spark discharge	van der Waals	experimental	Froeschke et al. (2003)
Si	simulation	van der Waals	molecular dynamics modeling	Hawa and Zacharaiah (2004)
colloidal nanoparticles	simulation	van der Waals solvation	molecular dynamics modeling	Qin and Fichthorn (2003)
colloidal nanoparticle	simulation	Coulomb	finite element modeling	Das and Bhattacharjee (2003)
CdTe	simulation	Coulomb van der Waals	Monte Carlo modeling	Sinyagin et al. (2005)
SiO_2	simulation	van der Waals	moment modeling	Suh et al. (2001)

ab initio molecular orbital and reaction rate theory (Zachariah and Tsang 1993, 1994). For collisions between larger clusters (e.g., consisting of 10 to 100s of atoms), classical molecular dynamics is often applied (Blaisten-Barojas and Zachariah 1992; Zachariah et al. 1994a, 1994b; Zachariah and Carrier 1999; Hawa and Zachariah 2004; Lümmen and Kraska 2004). *Ab initio* molecular orbital and molecular dynamics simulations have yielded much insight into the early time history of monomer clustering and the formation of incipient particles, including important information on clustering activation energies, cluster restructuring, clustering efficiencies and sticking coefficients.

For larger clusters and higher number densities, modeling approaches based on the aerosol dynamic equation (ADE) are typically used to represent the collision kinetics (Ulrich 1971; Ulrich et al. 1976). Approximate solution methods are commonly applied to solve the ADE in order to span a larger range of particle sizes. The most common approximate solution methods are based on moment and sectional models (Wu and Flagan 1988; Zachariah and Semerjian 1989; Landgrebe and Pratsinis 1990; Xiong and Pratsinis 1991, 1993; Pope and Howard 1997; Suh et al. 2001; Mueller et al. 2009). The moment method is typically applied while invoking assumptions regarding the size distribution of the particles where either a log-normal or a self-preserving profile is typically used. Hence, average particle properties are acquired, but with low computational costs. The sectional method groups particles by size bins where a constant particle size parameter such as the particle volume is assumed within each bin. Thus, sectional methods retain information about the individual particle properties but at high computational costs compared to the moment method. Other researchers have explored hybrid solution methods, for example integrating discrete relations for small clusters ($i = 1$ to 20) with sectional relations for the larger clusters (Gelbard et al. 1980; Wu and Flagan 1988; Langrebe and Pratsinis 1990). Mathematical modeling of agglomeration has also been carried out using finite element (Das and Bhattacharjee 2003), Monte Carlo (Sinyagin et al. 2005; Balthasar et al. 2005), and stochastic methods (Morgan et al. 2005, 2007).

Several experimental and modeling studies have examined the fundamental mechanisms important during nanoparticle clustering. Table 1 presents a brief introduction to some of the methods used to identify the forces important during interparticle collisions. These studies and others confirm that van der Waals interactions, electrostatic (Coulomb forces), and solid-state necking (particularly at high temperatures) are the most important processes to represent agglomeration and aggregation between nanoparticles.

2.2. Combustion Generated Nanoparticles

Particulates emitted from combustion processes are generally polydisperse with fractal structures (see Figure 1). The particle size distribution observed in combustion systems is a strong function of the local conditions (temperature, pressure, reactant concentrations, etc.). The size of the primary particles depends on the relative rate of coalescence and collision. Initially, primary particles in combustion systems are on the order of 5–20 nm in diameter, and the primary particles are considered approximately spherical in shape (Nakaso et al. 2001; Wooldridge et al. 2002; Mueller et al. 2009). The fractal structures are created by competition between the nucleation rate of the primary particles, the interparticle collision rate, and the coalescence or sintering rate. Nanoparticle cluster restructuring can also occur due to oxidation and other surface reactions and processes (di Stasio et al. 2002).

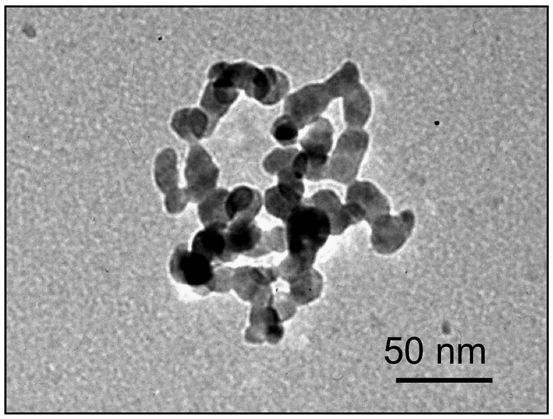

FIG. 1. Transmission electron micrograph image of flame-generated tin dioxide nanoparticle cluster.

The experimentally observed morphology of nanostructured soot agglomerates has been extensively studied using image analysis. Transmission electron microscopy (TEM) is the most common technique used for this purpose. TEM is typically used to acquire two-dimensional (2D) images of the agglomerates, which can be analyzed to extract information such as the average size of the primary particles, the number of primary particles in the agglomerate or aggregate, etc. Such 2D projections provides little information on the three-dimensional (3D) structure of the agglomerates; however, recent advances in TEM methods, such as electron tomography (Frank 1992; Radzilowski et al. 1997; Koster at al. 2000; Kohjiya et al. 2005; Adachi et al. 2007) and relative optical density (Tian et al. 2006, 2007) have extended the capabilities of TEM imaging to evaluate the 3D morphology of nanostructures.

Image processing is essential to extract quantitative information from TEM imaging data. Computer aided image analysis can easily evaluate a large number of particles and clusters, and it is much faster and less subjective than analysis conducted by individuals. Image analysis is commonly used to obtain the size distribution of nanoparticles (Fisker et al. 2000; Reetz et al. 2000) and fractal dimensions in 2D and 3D images (Köylü et al. 1995; Hayashi et al. 1999). Other parameters, such as the radius of gyration, linearity coefficient, aspect ratio, and particle chain length are also used to characterize the geometry of fractal nanoparticle structures (Fry et al. 2004).

3. THE INTEGRATED EXPERIMENTAL AND COMPUTATIONAL APPROACH

The current work presents a novel approach which combines 3D modeling and experimental data to identify the interactions that are important between nanoparticles. The method includes 3D TEM, image analysis, and computer simulation. Semi-stochastic or probabilistic modeling is used as the basis for simulating the nanoparticle interactions. Semi-stochastic mathematics is a powerful and robust means to model nanoparticle agglomeration because such methods do not require extensive information on material properties, environmental conditions, and reaction processes, which are often unavailable, particularly for nanoscale systems and combustion environments. Computer simulations based on probabilities can model agglomeration in 3D to predict complex nanoparticle cluster morphologies. Such techniques can be combined with 3D imaging and analysis from experimental data to analyze mechanisms of nanoparticle cluster formation. Based on the motivation to develop such analytical and predictive capabilities, the two objectives of this work were to develop the methods to simulate formation of nanoparticle clusters by semi-stochastic placement and to apply this method to identify the forces important during nanoparticle clustering in a representative combustion system.

For this initial foray into semi-stochastic modeling of combustion-generated particles, the modeling system considers interparticle collisions between monodisperse primary particles and fractal aggregates where Coulomb and Van der Waals forces are represented by relative probabilities. Coalescence and other particle growth mechanisms are not represented. Parametric studies are conducted to explore the effects of varying the relative strength of the Coulomb and Van der Waal forces on the predicted properties of 3D nanoparticle clusters. The mathematical concepts are then applied to identify the forces important during formation of combustion generated tin dioxide (SnO_2) nanoparticles.

3.1. Experimental Methods

Figure 2 shows the schematic of the combustion synthesis facility used to generate the combustion nanoparticulates analyzed in this work. Details on the particle sampling, burner characteristics and operating conditions can be found in Miller et al. (2005) and Bakrania et al. (2007a, 2007b). Briefly, in the current work, tin dioxide (SnO_2, cassiterite phase) particles were generated using a multi-element hydrogen-oxygen diffusion burner. Tetramethyltin (TMT, $Sn(CH_3)_4$) was introduced into the flame as a precursor for tin dioxide using argon as a carrier gas, yielding argon flow saturated with approximately 21% TMT on mole basis. TEM samples were acquired by thermophoretic deposition onto carbon-meshed copper grids at a fixed sampling location of 27 cm above the burner surface. Note that particle number densities are generally high in flame systems near the region of particle inception, which is located well below the sampling location (within 5 cm above the surface of the burner Bakrania et al. 2007a, 2007b) for the conditions and flame system studied in this work. For the SnO_2 system examined in this work, our prior studies indicate the primary means for particle restructuring and further growth is via agglomeration (Bakrania et al. 2007b). Particle sintering is several orders of magnitude (over 8 decades) slower at the sampling location than agglomeration, and there are no further tin sources for surface deposition or surface growth at the sampling location. Oxidation may still occur, but this should not lead to particle or agglomerate restructuring at the dimensions considered in this work. The SnO_2 particle

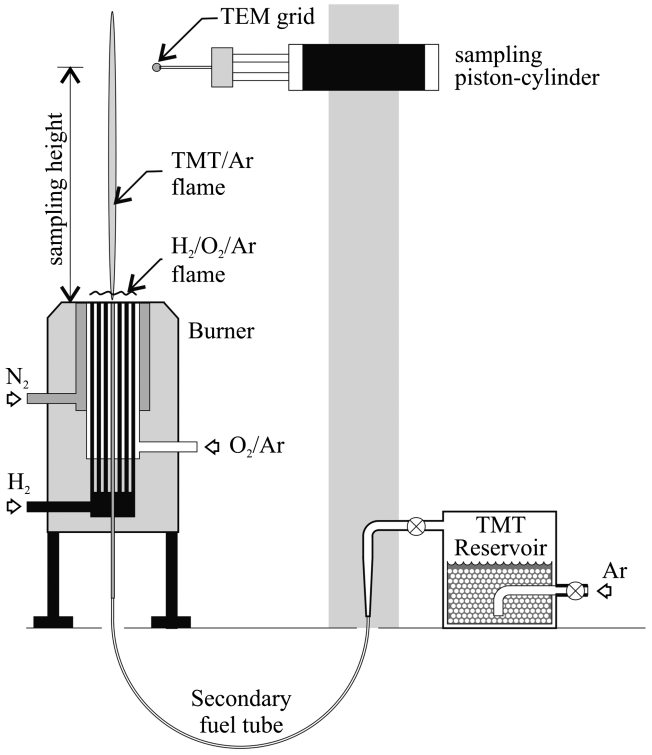

FIG. 2. Schematic of the combustion synthesis facility used to create the tin dioxide nanoparticles.

properties from this flame system have been extensively characterized in previous studies using 2D imaging (Bakrania et al. 2007a, 2007b), and the samples used for this study are typical for this combustion system and consistent with the results of the 2D samples. By using particles sampled from a fixed location, the formation and growth trajectories experienced by the particles can be considered identical.

TEM images of the particles were obtained using a JEOL 3011 High Resolution Electron Microscope. The specimen tilt capability was used to acquire 45 2D images at various planes of inclination with the tilt angle ranging from –55° to +55° in 2.5° increments. The 2D images acquired were aligned using the image processing and modeling software IMOD (the IMOD Home Page; Kremer et al. 1996). Image data were converted between Fourier and real spaces based on the electron tomographic technique (Frank 1992), and tomographic images were obtained from data conversion. The 3D cluster was then reconstructed and rendered by detecting the outline of the tomographic images using IMOD.

3.2. Computational Methods

A semi-stochastic method was used for the algorithm for generating the nanoparticle clusters. The model is semi-stochastic because the presence of particles depends on assigned probabilities in order to simulate the effect of different interactions. The computer simulation was used to generate 3D clusters of spherical nanoparticles with fixed particle diameters. The simulation was a 3D model with non-periodic boundaries. Each length of the domain cell was set at 1000 times the particle diameter so the cluster created in the simulation could not contact the boundary. During each simulation, a cluster consisting of N particles was formed, and 100 realizations of agglomerates for each value of N were computed and the results were averaged. Values of N from 10 to 100 were simulated. For each calculation, the initial primary particle was placed in the center of the cell. The agglomeration of nanoparticles was represented as a series of steps of single particle addition. The position of each new particle depended on the assigned probabilities. Based on the results of previous studies of nanoparticles clustering (see Table 1), two particle bonding criteria for forming agglomerates were considered representing van der Waals (Case 1) and Coulomb forces (Case 2). Case (1) is the addition of the next particle sticking to other particles in the cluster. Case (2) is the addition of the next particle sticking to the tip of a chain of particles in the cluster.

Case (1) represents the short-range van der Waals forces that make particles stick together when two particles collide. Figure 3a shows schematically how Case (1) is implemented in the simulations. For each particle addition step, a particle within the existing cluster is randomly chosen as the binding site. The position of the new particle is chosen using a random angle around the particle in the cluster. If the new particle overlaps with other particles in the cluster, the new particle is not added to the cluster and the process is restarted.

Case (2) represents the attractive forces due to dipoles or charges concentrated on the tip of a chain of particles and the repulsive forces of the inner part of a cluster. These long-range forces cause bonding to occur at the tip of a chain of particles. Figure 3b shows schematically how Case (2) is implemented in the simulations. For a cluster with two tip particles in the computational domain, one tip particle is randomly selected as the site for the addition of the new particle. The position of the new particle is determined using a random angle around the hemisphere of the tip particle. The assumption of the new particle sticking at an angle in the hemisphere of the tip particle is based in part by experimental observation (Onischuk et al. 2000). While Onischuk et al. (2000) considered larger particles than those studied in this work ($\sim$10 μm), it is well known that SnO_2 nanoparticles will readily develop a charge depletion layer upon exposure to oxygen and other gases (Miller et al. 2006 and references therein). Thermionic charging may also occur in flame systems. While charge transfer can be incorporated into the model using probabilities there are no data on the electron transfer rates at flame temperatures for nanoparticles and agglomerates. Thus, Case (2) represents the limiting condition where the charge is located on the tip and no charge transfer occurs within the agglomerate. As with Case (1), if the new particle overlaps with other particles in the cluster, the new particle is not added to the cluster, and the process is restarted.

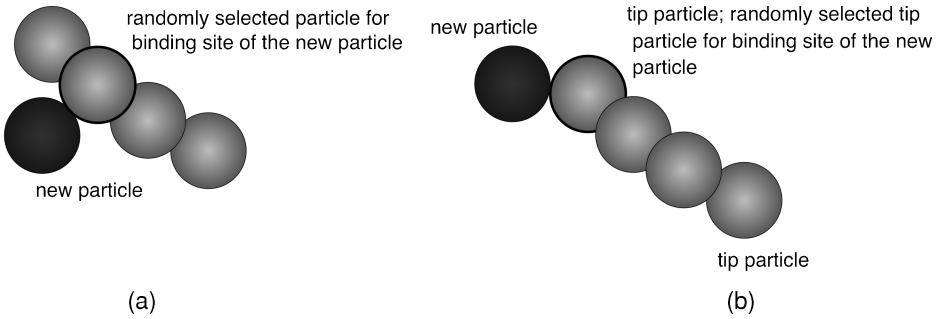

FIG. 3. Schematic representing the (a) Case 1 binding method (van der Waals interactions) and (b) Case 2 binding method (Coulomb forces). The gray particles are particles existing within the computational boundary, and the black particle is the new particle searching for a binding site. The gray particle circled in black is the randomly chosen particle for binding.

P1 is the probability of Case (1) occurring during agglomerate formation, and P2 is the probability of Case (2). The summation of P1 and P2 is 1 because there are only two bond criteria assigned in the simulation. By varying the assigned probabilities of Case (1) and Case (2), the combination of forces during the formation of agglomerates can be simulated. The cluster forming process is not a real-time simulation, and only the probabilities and the geometry of a specific final cluster are analyzed.

3.3. Image Analysis

Radius of gyration, aspect ratio, main chain length, fractal dimension and fractal prefactor are used to characterize the geometric properties of the 3D nanoparticle clusters from the experiments and simulations. For a specific cluster, radius of gyration, R_g, is used to characterize the overall size of the cluster. Aspect ratio is used to estimate the shape of the cluster in terms of the ratio of the three major axes of the fitted ellipsoid. Main chain length, L_m, is used to determine the maximum chain length in the cluster. Fractal dimension, D_f, is used to characterize the compactness of the cluster. Each geometric property was determined as follows.

Radius of gyration, R_g, of a cluster is a measure of its overall size, which is expressed as

$$R_g^2 = \frac{\int r^2 \rho(\vec{r}) d\vec{r}}{\int \rho(\vec{r}) d\vec{r}} \quad [1]$$

where r is the radial distance measured from the cluster center of mass and $\rho(r)$ is the cluster mass density. The denominator is equal to the total cluster mass. The density of each particle is assumed constant.

From Fry et al. (2004), the shape of any object can be characterized by the moment of inertia tensor, T_I, with components

$$T_{ij} = \int \rho(\vec{r}) q_i q_j d\vec{r} \quad \text{for} \quad i, j = 1, \ldots, d, i \neq j \quad [2a]$$

$$T_{ij} = \int \rho(\vec{r}) q_i q_j d\vec{r} \quad \text{for} \quad i, j = 1, \ldots, d, i = j \quad [2b]$$

where $q_i = x, y, z$ for $i = 1, 2, 3$ respectively, and x, y, z are coordinate values. By diagonalizing and dividing by the total cluster mass, the squares of principal radii of gyration R_i^2, for $i = 1, \ldots, d$, can be obtained. Then the shape and overall size of the particle are related by

$$R_g^2 = \frac{1}{2}\left[R_1^2 + R_2^2 + R_3^2\right] \quad [3]$$

The principal radii of gyration and axes lengths of the fitted 3D ellipsoid are related by

$$R_i^2 = \frac{2}{5}\left[d_j^2 + d_k^2\right] \quad [4]$$

where $d_i = a, b, c$ for $I = 1, 2, 3$ respectively, and a, b, c are three main axes of the fitted ellipsoid. Solving for di yields

$$d_i^2 = \left[\frac{2}{5}(1 - 2\delta_{i1})R_1^2 + (1 - 2\delta_{i2})R_2^2 + (1 - 2\delta_{i3})R_3^2\right]^{\frac{1}{2}} \quad [5]$$

where δ_{ij} is the Kronecker delta and d_i corresponds to axes a, b, c for $I = 1, 2, 3$. The aspect ratios a_b (a/b) and a_c (a/c) can then be obtained from Equation (5).

Main chain length, L_m, is the length along the actual path between the two most distant particles in a cluster. L_m is calculated using the Floyd-Warshall All-Pairs-Shortest-Path algorithm (Cormen et al. 1990). The main chain length and radius of gyration are reported as dimensionless values in this work by normalization using the radius of the particle, r. L_m is measured from the end point of a particle, through the particle center, to the end point of another particle. For example, if N is one, Lm/r is 2.

The fractal dimension, D_f, is determined using the following expression (Friedlander 2000),

$$N = A\left(\frac{R_i}{r}\right)^{D_f} \quad [6]$$

where r is the radius of the primary particle and A is the fractal prefactor and a dimensionless constant. For the simulations, average values for D_f and A are determined by averaging over many agglomerates with the same N. For compact agglomerates, D_f is close to 3, and for chain-like structures, D_f is close to 1.

The computationally generated 3D agglomerates and the 3D reconstructions of the experimentally observed agglomerates were analyzed using identical methods. Uniform $4 \times 4 \times 4$ distributed grids were dispersed in each unit cubic to calculate R_g, a_b, a_c, and L_m. Comparison of the simulation results and experimental data allows values for P1 and P2 to be determined, and the forces important during agglomeration can thus be determined indirectly.

4. RESULTS

4.1. Simulation Results for Varying Interparticle Forces

Figure 4 shows the effects of the relative values of P1 and P2 on the average aspect ratio a_b, for values of $N = 20$, 40, 60, 80, and 100. (Recall $P_2 = 1 - P1$.) Results for a_c are systematically higher than the values for a_b for all values of P1; however, the results exhibit similar trends and are not included here. Both aspect ratios decrease as the number of particles in the cluster increases, and both aspect ratios decrease as the probability of Case 1 bonding (representing van der Waals forces) increases. Figure 5 presents the notched-box plots of the effects of P1 on the aspect ratio ab for $N = 20$, 60, and 100. Each notched box has lines at the lower quartile, median, and upper quartile values. Each notched box also has whiskers which are lines extending from each end of the box to show the extent of the rest of the data in 1.5 times the interquartile range. Outliers (denoted as plus signs in the figures) are data with values beyond the ends of the whiskers. If the notches in the box plot do not overlap, one can conclude with 95% confidence that the true medians differ (McGill et al. 1978). For example, results from Figure 5 shows that when P1 is larger than approximately 0.6, there is no significant change in the median value of a_b for the 3 values of N presented. Additionally, a wider range between whiskers, especially with larger values of P1, indicates larger variation in the data. Data distribution can also be observed in notched-box plots, and Figure 5 shows asymmetric data distribution. Extended data deviation in larger values results in the averaged values in Figure 4 being greater than the median values in Figure 5.

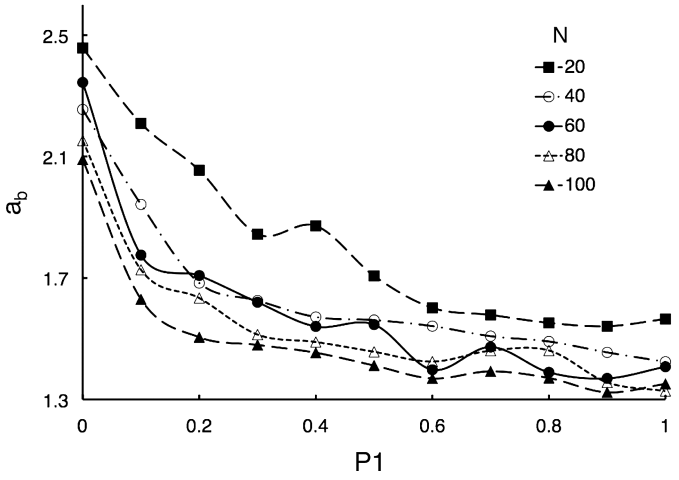

FIG. 4. Simulation results for a_b as a function of P1 for cluster sizes N = 20, 40, 60, 80, and 100.

Figures 6 and 7 show the effects of P1 on average main chain length, L_m/r, and normalized main chain length, $L_m/(Nr)$, for values of $N = 20$, 40, 60, 80, and 100. L_m/r increases with decreasing values of P1 and increasing values of N. The normalized main chain length also increases with decreasing values of P1; however, $L_m/(Nr)$ decreases with increasing values of N. P1 = 0 is the special case where new particles always stick to the tip particles, and only one chain-like structure with $L_m/(Nr) = 2$ is formed. Note that the curves do not collapse to a single trend when normalized by the number of particles in an agglomerate, and hence the normalized mean chain length is not simply an inverse function of N. Figure 8 shows the notched box plots of the effects of P1 on L_m/r for $N = 20$, 60, and 100. The range between whiskers decreases with increases in P1. However, unlike aspect ratio, notches in the box plots for L_m/r only overlap over a small range of values for P1 (e.g., P1 = 0.7–0.8, $N = 100$).

Figure 9 shows the effects of P1 on the average radius of gyration normalized by particle radius, R_g/r, for values of $N = 20, 40, 60, 80$, and 100. R_g/r increases with decreasing values of P1 and with increasing values of N. Notched box plots of R_g (not shown here) yield results similar to main chain length, where as values for P1 and N increase, the range between whiskers decreases, with no overlap between notches at lower values of P1.

The simulation results were also examined to determine if the predicted structures were self-similar by considering the $\log(N)$ data as a function $\log(R_g/r)$. The results are presented in Figure 10 and the linearity of the data indicates the structures are self-similar. From Equation (6), the fractal dimension, D_f, and fractal prefactor, A, can be obtained from the linear fit of $\log(R_g/r)$ versus $\log(N)$. Using regression analysis, D^f and A were determined for each value of P1, and the results are presented in Figure 11. D_f increases from 1.8 to ~3 and A decreases from ~0.84 to 0.4 as P1 increases from 0 to 1. In order to compare with the fractal dimension information based on 2D imaging (which is often the basis for the results reported in the literature), Figure 11 also presents results for D_f and A based on 2D projections of the simulated 3D structures (projected onto the z-plane). For the 2D results, D^f increases from 1.8 to 3.3 and A decreases from 1.35 to 0.36 with increasing values of P1 from 0 to 1.

It is valuable to explore relationships that can link 2D data to 3D agglomerate geometric information. Figure 12 presents

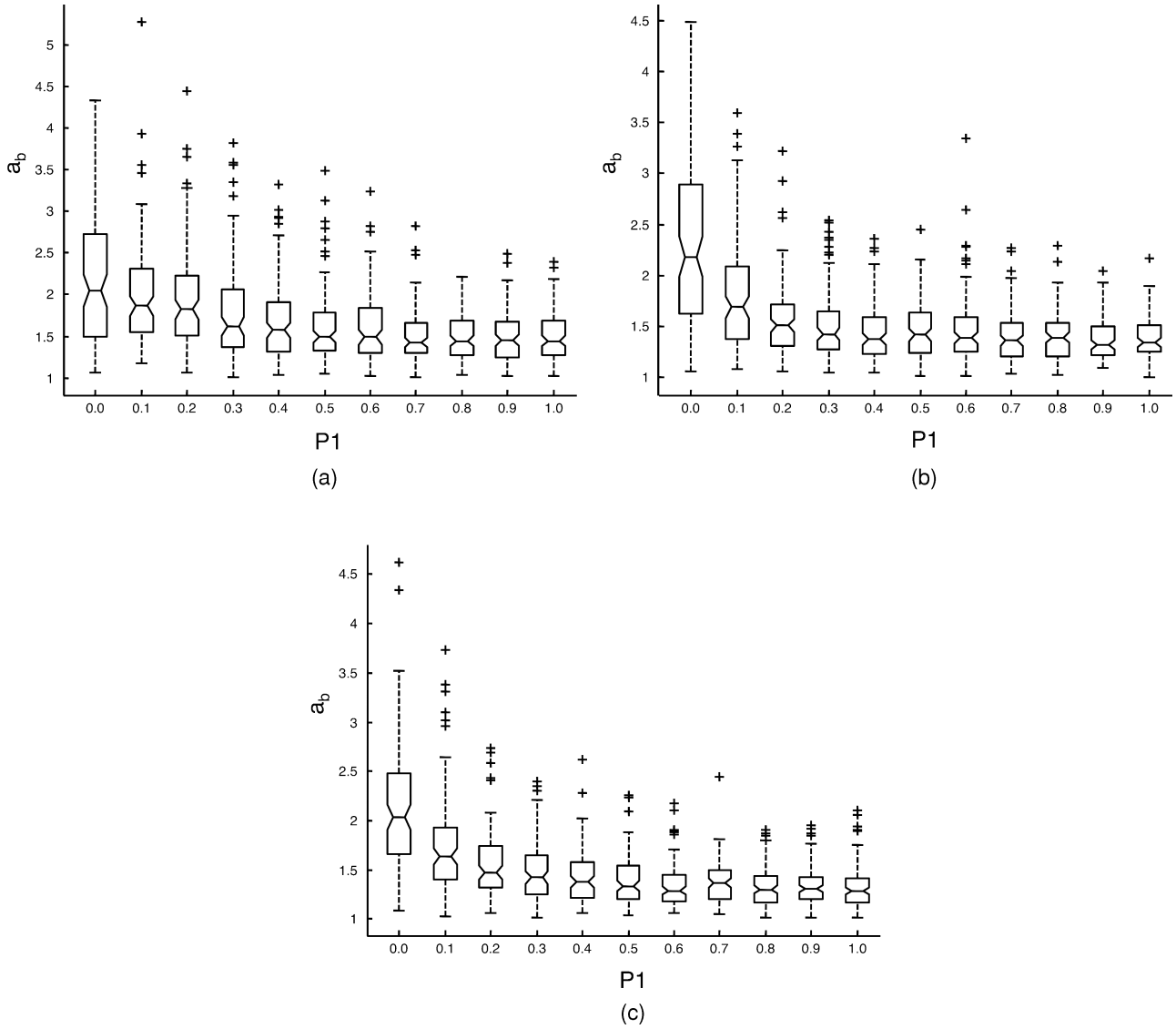

FIG. 5. Simulation results for notched box plots of the effect of P1 on aspect ratio a_b for $N =$ (a) 20, (b) 60, and (c) 100.

the relationship between the ratio of L_m in 2D to R_g in 3D as a function of the cluster size and varying clustering probabilities. For a specific combination of clustering forces, the $L_{m,2D}/R_{g,3D}$ ratio shows a positive relationship with N; with lower values of P1 showing higher sensitivity to the number of particles in the cluster. Thus at conditions with known particle interactions and cluster size, 3D R_g data can be determined from 2D measurements of L_m.

4.2. Image Analysis of SnO_2 Nanoparticle Clusters

Figures 13 shows TEM images of the distinct SnO_2 particle cluster with $N = 45$ sampled from the combustion system. The tilt angles used for the images were -55°, 0°, and $+55^\circ$. As seen in the images, considerably different 2D projections are observed from the same cluster for different tilt angles. Figures 14 presents 2D projections of the reconstructed 3D structures of the clusters from Figures 13. The projected 2D images from the 3D reconstruction are presented for -55°, 0°, $+55^\circ$, $+110^\circ$, and $+165^\circ$ tilt angles. Note the 2D projected images based on the 3D reconstructions correctly reproduce the TEM images of Figures 13 for equivalent tilt angles.

TEM image and 3D structure image of another cluster with $N = 16$ are reported in supplemental information section as shown in Figure S1 and S2 for brevity.

Table 2 presents the results from the image analysis of the flame-generated SnO_2 clusters presented in Figures 13 and S1. The analysis yields $N = 45$ and $r = 21.5$ [pix] for Cluster I and $N = 16$ and $r = 20.5$ [pix] for Cluster II. Comparing the results for the geometric features of the nanoparticles clusters

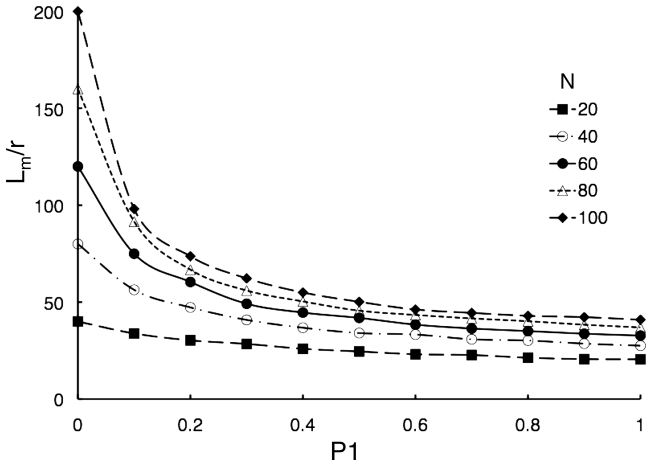

FIG. 6. Simulation results of the effect of P1 on average main chain length normalized by particle radius, L_m/r, for cluster sizes $N = 20$, 40, 60, 80, and 100.

TABLE 2
Results of image analysis of SnO_2 nanoparticle clusters.

Parameter	Cluster I	Cluster II
N	45	16
scale [pix/nm]	2.3	2.3
r [pix]	21.5	20.5
r [nm]	9.3	8.9
L_m[pix]	1610.3	536.8
L_m[nm]	700.1	233.4
R_g[pix]	190.2	99.3
R_g[nm]	82.7	43.2
L_m/r	74.9	26.2
R_g/r	8.8	4.8
estimated P1 by L_m/r	0–0.1	0.2–0.3
estimated P1 by R_g/r	0–0.1	0–0.3

from the experiments with the results from the simulations, if the values from the experimental imaging are located within the range of the boxes, P1 can be determined. Estimated ranges of P1 for the two nanoparticles clusters are shown in Table 2 based on comparison of the normalized values for mean chain length and radius of gyration. The implication of these results are discussed below.

5. DISCUSSION

5.1. Parametric Studies of Simulation Parameters

By varying the probabilities representing these forces, different combinations of P1 and P2 simulate different effects of van der Waals and Coulomb forces. The simulation results (Figures 4–12) demonstrate that Coulomb forces (Case 2) are responsible for elongated agglomerates while van der Waals forces (Case 1) yield particles with more compact structure. Specifically agglomerates tend to form larger looser structures with larger aspect ratios, longer mean chain length and higher radius of gyration when P2 is higher or systems where Coulomb forces dominate. Particles form more compact and dense clusters with smaller aspect ratios, main chain length, and radius of gyration when P1 is higher or systems where van der Waal forces are more important. The attractive Coulomb force concentrated on the tip particles is responsible for elongated clusters, and with increasing N, new particles have more opportunities to stick to particles in the cluster which are farther from the major axes and not part of the main chain, so the aspect ratio and the normalized main chain length, $L_m/(Nr)$, both decrease with increasing N. Without the strong forces at the tip, new particles bind to other parts of the cluster due to van der Waals forces and form more compact structures.

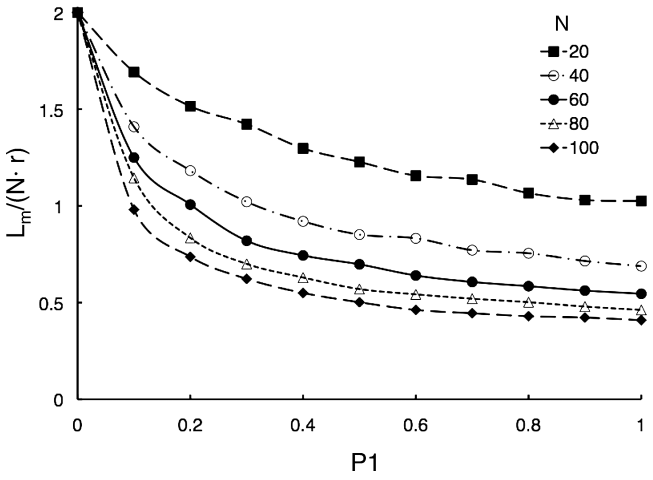

FIG. 7. Simulation results of the effect of P1 on normalized main chain length, $L_m/(Nr)$, for cluster sizes $N = 20$, 40, 60, 80, and 100.

The box plots (Figures 5 and 8) indicate the variety of shapes the agglomerates can form. For lower values of P1, the whiskers of the boxes are larger, which indicates that the shape of the clusters is more variable when controlled by the strong effects of Coulomb forces on the tip particles. For higher values of P1, the smaller whiskers on the box plots indicate more uniform morphology is observed. For aspect ratio (Figure 5), the boxes overlap over a wide range of P1 especially at smaller values of N indicating aspect ratio is not a good parameter to uniquely identify the forces important during particle clustering. However, normalized mean chain length and radius of gyration do not exhibit significant overlap in the boxes except for small values of N. As a consequence L_m/r and R_g/r are useful to characterize the forces important during the formation of larger agglomerates and aggregates. For smaller clusters (e.g., $N < 20$), comparison with experimental data for L_m/r and R_g/r can identify a range of probabilities, but may not yield a unique combination.

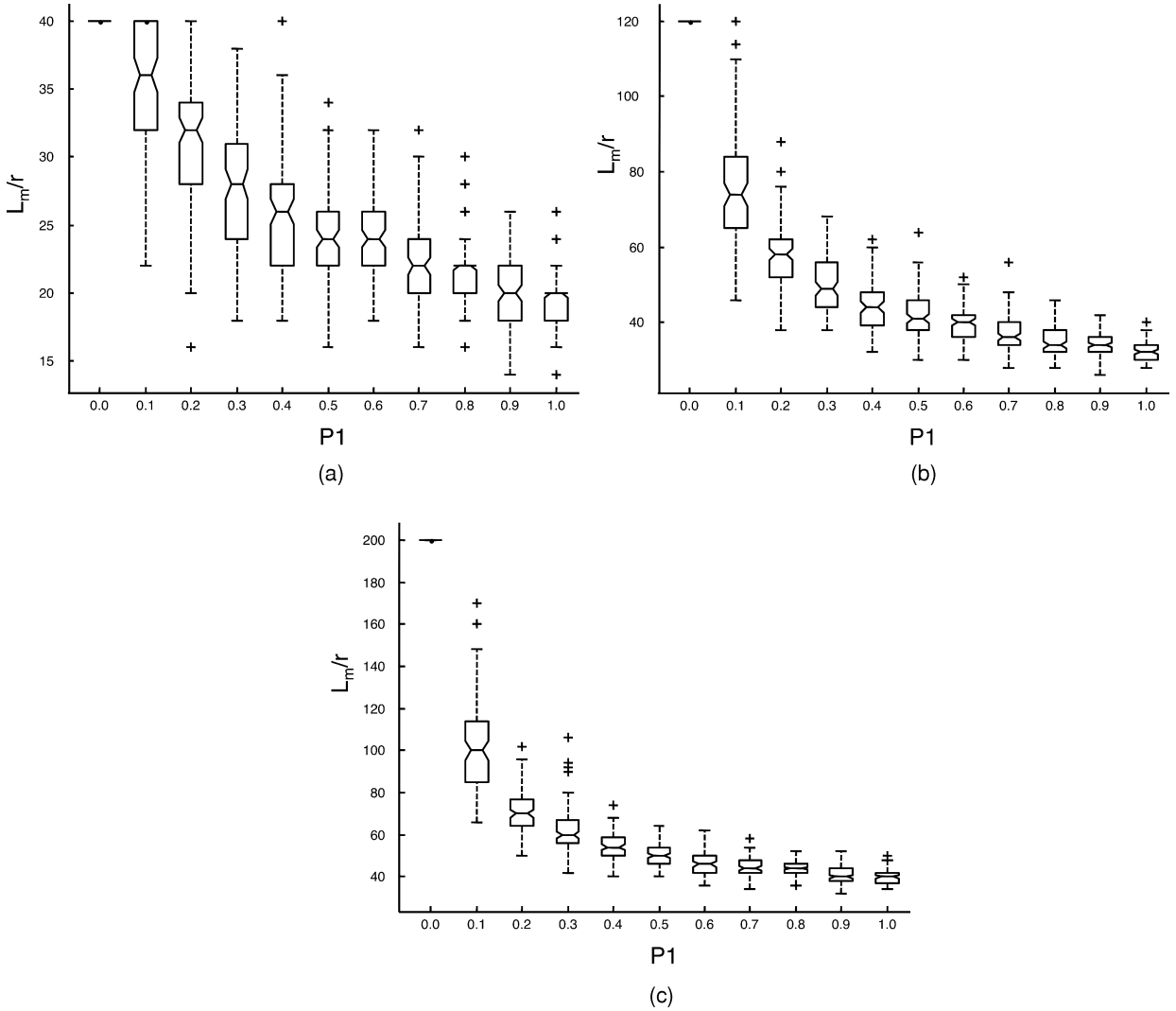

FIG. 8. Simulation results for notched box plots of the effect of P1 on L_m/r when $N =$ (a) 20, (b) 60, and (c) 100.

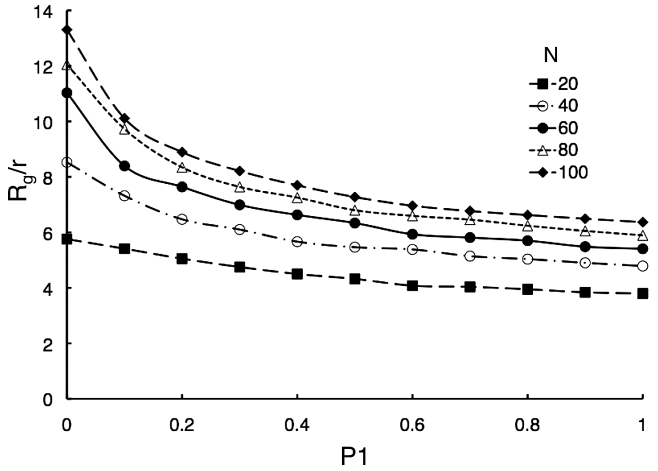

FIG. 9. Simulation results for the effects of P1 on average radius of gyration, R_g/r, for cluster sizes $N = 20$, 40, 60, 80, and 100.

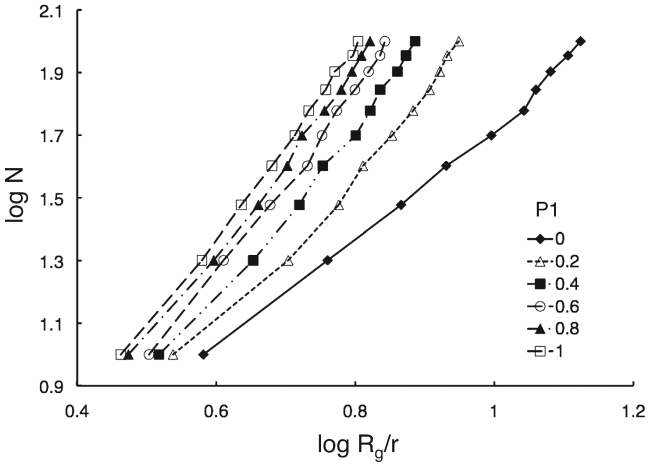

FIG. 10. Simulation results to evaluate the self-similarity of the predicted particle clusters.

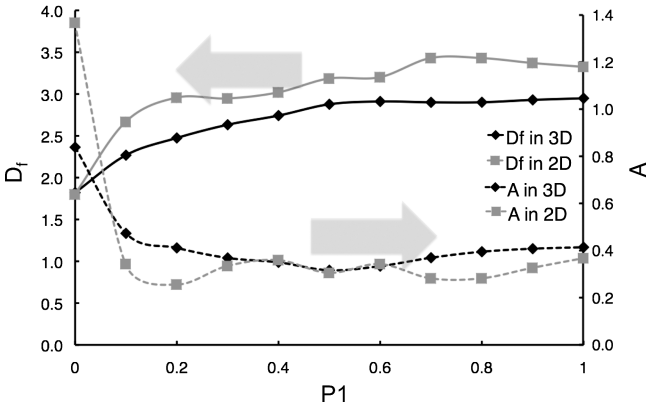

FIG. 11. Simulation results for fractal dimension D_f and fractal pre-factor A as a function of P1 using 3D data and 2D projections of the 3D data.

The simulation results for $\log(R_g/r)$ vs. $\log(N)$ indicate the agglomerates are self-similar structures (Figure 10). The results (Figure 11) also show the fractal dimension is a weak function of the interparticle forces as P1 increases to >0.5. The fractal prefactor is an even weaker function of the interparticle forces except for systems dominated by Coulomb interactions (P1 < 0.2). Thus the fractal parameters are not good variables to uniquely characterize particle interactions. The results presented in Figure 11 also demonstrate the systematic error that can be introduced, when deriving fractal dimensions from 2D projections, where D^f,2D was larger than D^f,3D for all values of P1 > 0.

D_f values typically range between 1.6–1.9 for combustion generated carbonaceous soot nanoparticles (Köylü et al. 1995; Sorenson 2001; Yazicioglu et al. 2001; Hu and Köylü 2004; Tian et al. 2006; Maricq 2007). The simulation results presented in Figure 11 are well within this range, which is extremely promising given the simulation currently considers clustering of monodisperse primary particles representing only two clustering mechanisms. Values for fractal prefactor for combustion generated nanoparticles are less consistent with values of A = 1 – 3 reported in the literature (Köylü et al. 1995; Sorenson 2001; Yazicioglu et al. 2001; Tian et al 2006). Figure 11 also shows the error in fractal prefactor that can be introduced from using 2D projections to derive values for A. Unlike D_f, the fractal prefactor does not systematically deviate between 2D and 3D determinations and the differences between A_{2D} and A_{3D} can be quite high at lower values of P1.

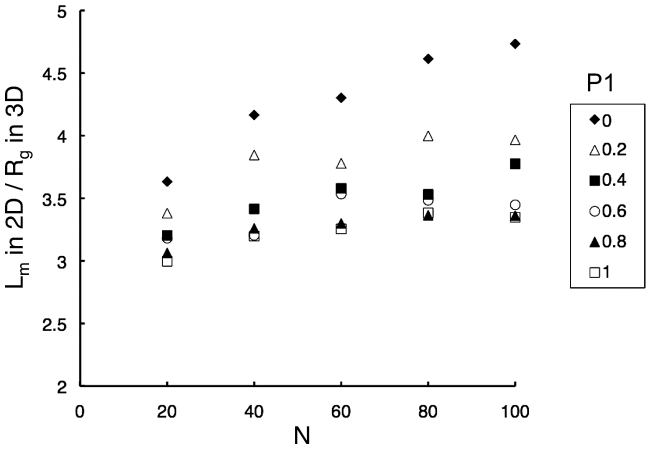

FIG. 12. Simulation results of the effects of P1 on the ratio of L_m in 2D to R_g in 3D for cluster sizes $N = 20$, 40, 60, 80, and 100.

5.2. Analysis of Experimental Imaging Data

The experimental data (Figures 13 and S1) and the image reconstruction results (Figures 14 and S2) demonstrate the three dimensional nature of the combustion-generated SnO_2 agglomerates. The nanoparticle clusters yield different 2D projections based on the orientation of the image. Analysis of 2D TEM images using a single projection angle does not contain sufficient information to reconstruct the 3D shape of the SnO_2 clusters. Additionally, 2D projected images can lead to incorrect assumptions regarding the real cluster geometry. 3D TEM provides further structural understanding in real space. However, the simulation results show under certain conditions, quantitative links can be made between 2D and 3D features.

The forces governing the formation of a specific cluster can be estimated by comparing experimental data derived from the 3D TEM imaging and the 3D modeling results for L_m/r and R_g/r. Comparing the experimental results of Table 2 with the simulation results, P1 for Cluster I is estimated between 0 and 0.1 based on both L_m/r and R_g/r. The results indicate that the Coulomb forces dominate during the formation of the SnO_2 particle cluster. For Cluster II, P1 is estimated between 0.2–0.3 based on the values for L_m/r, and P1 is estimated between 0–0.3 based on the values for R_g/r. As noted earlier, for smaller agglomerates ($N < 20$) various combinations of P1 and P2 can result in similar morphologies, hence the larger range of probabilities assigned to this smaller cluster, where $N_{\text{Cluster II}} = 16$).

The results for the forces governing the SnO_2 nanoparticle cluster formation are consistent with other studies of agglomeration of combustion-generated particulates. For example, Onischuk et al. (2000) studied agglomeration through experimental observation of particle/agglomerate interactions of carbonaceous soot aerosols and silicon aerosols generated through silane pyrolysis. They found that "Coulomb interactions are significant during the sticking process and, in particular, they are responsible for the fractal dimension." The authors also found the type and extent of dipole charge varied between the two materials studied.

The radii of gyration determined from the simulations and from the reconstruction of the TEM images are also consistent with other measurements of combustion-generated particulates. For example, di Stasio et al. (2002) studied clusters of carbon particles formed in an atmospheric pressure ethylene diffusion flame using light scattering. The authors found the

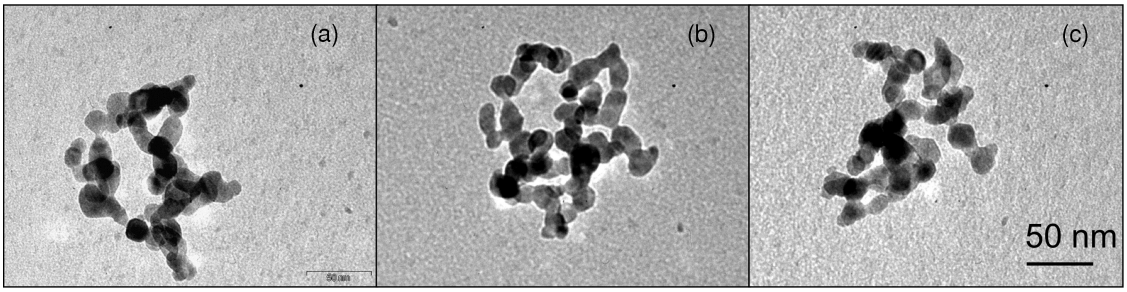

FIG. 13. TEM images of agglomerate I at different tilt angles: (a) −55°, (b) 0°, and (c) +55°.

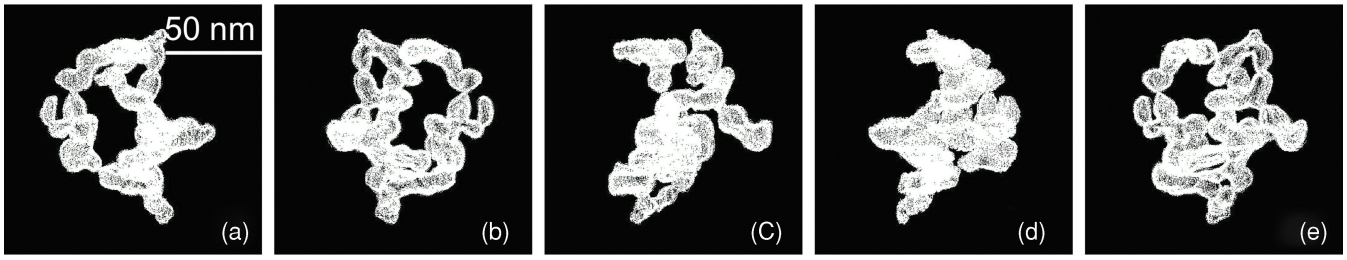

FIG. 14. 2D projections of 3D model of agglomerate I at different angles of orientation: (a) −55°, (b) 0°, (c) +55°, (d) +110°, and (e) 165°.

soot particles formed fractal structures where R_g varied from 25 to 375 nm based on the residence time of the particles in the flame. The measured values for R_g for Cluster I (83 nm) and II (43 nm) (Table 2) and the computed range of values shown in Figure 9 (normalized) are consistent with the light scattering data.

6. CONCLUSIONS

A new method based on image analysis, 3D model reconstruction, and computer simulation was developed to identify factors important during clustering of SnO_2 nanoparticles. The approach used probabilistic techniques, along with image analysis, rather than first physiochemical principles, to predict and analyze mechanisms of cluster formation. While some of the general conclusions of the study are well documented in the literature, this is the first attempt to model and analyze particle clustering using such methods. As a consequence, the conclusions of the study are valuable as independent verification of key particle clustering concepts and as validation of the technical methods used. Additionally, this study presents the first characterization of tin dioxide nanoparticle clustering. Specifically, the branchy structures observed for the SnO_2 clusters were attributable to strong Coulomb forces, with minimal van der Waals interactions.

Application of the model over a range of probabilities representing varying levels of Coulomb and van der Waals forces showed that Coulomb forces concentrated on the tip of particle clusters inevitably lead to formation of long chain-like shapes, creating branchy nanoparticle clusters. Coulomb forces were also found to be responsible for greater variability in the shapes of clusters. Particles tended to form more uniform and more compact and smaller clusters when van der Waals forces dominated. The simulation results indicated the clusters formed self-structures for the combinations of interactions considered. The simulation results showed radius of gyration and main chain length are good parameters to characterize the forces governing 3D cluster formation, while fractal dimensions and prefactors are not. L_m and R_g also provide a means to link 2D and 3D features of the particle clusters under certain conditions.

The approach demonstrated in this work combines experimental data, image reconstruction and semi-stochastic modeling, and is a powerful means to analyze particle clusters, providing new insight without high computational costs. While the approach must be expanded to consider polydisperse systems, cluster-cluster interactions, charge transfer, and other agglomeration formation and restructuring mechanisms, these aspects can each be represented using the semi-stochastic modeling approach demonstrated here and are important areas for future consideration. The potential impact of such an approach is high. For example, this approach can be applied to provide new understanding for diverse material systems such as what forces are controlling the formation of highly ordered structures in flames, such as rods and whiskers, as opposed to fractal agglomerates and aggregates, without requiring the significant thermophysical input data that other approaches require. With greater resolution, this method may provide even higher level of detail such as the charge state of the nanoparticle clusters and the effects of charge distribution on particle clustering. Additionally, such methods can be the basis for developing predictive models for particle formation that can bridge the gap between detailed chemical modeling and nanoparticle interaction

while retaining critical information on particle geometry. Lastly, other methods to uniquely connect 2D and 3D geometric features of the clusters can be easily explored with this modeling approach.

REFERENCES

Adachi, K., Chung, S. H., Friedrich, H., and Buseck, P. R. (2007). Fractal Parameters of Individual Soot Particles Determined using Electron Tomography: Implications for Optical Properties, *J. Geophys. Res. D.* 112:D14202:1–10.

Bakrania, S. D., Miller, T. A., Perez, C., and Wooldridge, M. S. (2007a). Combustion of Multiphase Reactants for the Synthesis of Nanocomposite Materials, *Combust. Flame*. 148:76–87.

Bakrania S. D., Perez C., and Wooldridge, M. S. (2007b). Methane-Assisted Combustion Synthesis of Nanocomposite Tin Dioxide Materials, *Proc. Combust. Inst.* 31:1797–1804.

Balthasar, M., Frenklach, M., Boris, J., Oran, E., Roth, P., Rosner, D. E., and Dobbins, R. (2005). Monte-Carlo Simulation of Soot Particle Coagulation and Aggregation: The Effect of a Realistic Size Distribution, *Proc. Combust. Inst.* 30:1467–1475.

Blaisten-Barojas, E., and Zachariah, M. R. (1992). Molecular-Dynamics Study of Cluster Growth by Cluster-Cluster Collisions, *Phys. Rev. B.* 45:4403–4408.

Cormen, T. H., Leiserson, C. E., and Rivest, R. L. (1990). *Introduction to Algorithms*. The MIT Press, Cambridge.

Das, P. K., and Bhattacharjee, S. (2003). Electrostatic Interactions between Nanoparticles in Confined Spaces: Influence of Confining Wall Roughness, *Proc. Intl. Conf. MEMS, NANO, Smart Systems*. 0-7695-1947-4/03:1–5.

di Stasio, S., Konstandopoulos, A. G., and Kostoglou, M. (2002). Cluster-Cluster Aggregation Kinetics and Primary Particle Growth of Soot Nanoparticles in Flame by Light Scattering and Numerical Simulations, *J. Colloid Interface Sci.* 247:33–46.

Fisker, R., Carstensen, J. M., Hansen, M. F., Bødker, F., and Mørup, S. (2000). Estimation of Nanoparticle Size Distributions by Image Analysis, *J. Nanopart. Res.* 2:267–277.

Frank, J., ed. (1992). *Electron Tomography: Three-Dimensional Imaging with the Transmission Electron Microscope*, Plenum Press, New York.

Friedlander, S. K. (2000). *Smoke, Dust, and Haze: Fundamentals of Aerosol Dynamics*. Oxford University Press, New York.

Froeschke, S., Kohler, S., Weber, A. P., and Kasper, G. (2003). Impact Fragmentation of Nanoparticle Agglomerates, *J. Aerosol Sci.* 34:275–287.

Fry, D., Mohammad, A., Chakrabarti, A., and Sorensen, C. M. (2004). Cluster Shape Anisotropy in Irreversibly Aggregating Particulate Systems, *Langmuir*. 20:7871–7879.

Gelbard, F., Tambour, Y., and Seinfeld, J. H. (1980). Sectional Representations for Simulating Aerosol Dynamics, *J. Colloid Interface Sci.* 76:541–556.

Hawa, T., and Zachariah, M. R. (2004). Molecular Dynamics Study of Particle–Particle Collisions between Hydrogen-Passivated Silicon Nanoparticles, *Phys. Rev. B.* 69:035417:1–9.

Hayashi, S., Hisaeda, Y., Asakuma, Y., Aoki, H., Miura, T., Yano, H., and Sawa, Y. (1999). Simulation of Soot Aggregates Formed by Benzene Pyrolysis, *Combust. Flame.* 117:851–860.

Hu, B., and Köylü, Ü. Ö. (2004). Size and Morphology of Soot Particulates Sampled from a Turbulent Nonpremixed Acetylene Flame, *Aerosol Sci. Tech.* 38:1009–1018.

The IMOD Home Page, http://bio3d.colorado.edu/imod/index.html, Boulder Lab For 3D Electron Microscopy of Cells, University of Colorado.

Kohjiya, S., Katoh, A., Shimanuki, J., Haseqawa, T., and Ikeda, Y. (2005). Three-Dimensional Nano-Structure of In Situ Silica in Natural Rubber as Revealed by 3D-TEM/Electron Tomography, *Polymer*. 46:4440–4446.

Koster, A. J., Ziese, U., Verkleij, A. J., Janssen, A. H., and de Jong, K. P. (2000). Three-Dimensional Transmission Electron Microscopy: A Novel Imaging and Characterization Technique with Nanometer Scale Resolution for Materials Science, *J. Phys. Chem. B* 104:9368–9370.

Köylü, Ü. Ö., Faeth, G. M., Farias, T. L., and Carvalho, M. G. (1995). Fractal and Projected Structure Properties of Soot Aggregates, *Combust. Flame*. 100:621–633.

Kremer, J. R., Mastronarde, D. N., and McIntosh, R. (1996). Computer Visualization of Three-Dimensional Image Data using IMOD, *J. Struct. Bio.* 116:71–76.

Landgrebe, J. D., and Pratsinis, S. E. (1990). Discrete-Sectional Model for Particulate Production by Gas-Phase Chemical Reaction and Aerosol Coagulation in the Free-Molecular Regime, *J. Colloid Interface Sci.* 139:63–86.

Lümmen, N., and Kraska, T. (2004). Investigation of the Formation of Iron Nanoparticles from the Gas Phase by Molecular Dynamics Simulation, *Nanotech.* 15:525–533.

Maricq, M. M. (2007). Coagulation Dynamics of Fractal-Like Soot Aggregates, *J. Aerosol Sci.* 38:141–156.

McGill, R., Tukey, J. W., and Larsen, W. A. (1978). Variations of Boxplots. *The Amer. Stat.* 32:12–16.

Miller, T. A., Bakrania, S. D., Perez, C., and Wooldridge, M. S. (2005). A New Method for Direct Preparation of Tin-Dioxide Nanocomposite Materials, *J. Mater. Res.* 20:2977–2987.

Miller, T. A., Bakrania, S. D., Perez C., and Wooldridge, M. S. (2006). Nanostructured Tin Dioxide Materials for Gas Sensor Applications. in *Functional Nanomaterials*, E. Rosenberg and K. E. Geckeler, eds., American Scientific Publishers, California, chap. 29, pp. 453–475.

Mueller, M. E., Blanquart, G., and Pitsch, H. (2009). A Joint Volume-Surface Model of Soot Aggregation with the Method of Moments, *Proc. Combust. Inst.* 32:785–792.

Morgan, N., Wells, C., Kraft, M., and Wagner, W. (2005). Modelling Nanoparticle Dynamics: Coagulation, Sintering, Particle Inception and Surface Growth, *Combust. Theory Model.* 9:449–461.

Morgan, N., Kraft, M., Balthasar, M., Wong, D., Frenklach, M., and Mitchell, P. (2007). Numerical Simulations of Soot Aggregation in Premixed Laminar Flames, *Proc. Combust. Inst.* 31:693–700.

Nakaso, K., Fujimoto, T., Seto, T., Shimada, M., Okuyama, K., and Lunden, M. M. (2001). Size Distribution Change of Titania Nano-Particle Agglomerates Generated by Gas Phase Reaction, Agglomeration, and Sintering, *Aerosol Sci. Tech.* 35:929–947.

Nizich, S. V., Pope, A. A., Driver, L. M., and the Pechan-Avanti Group. (2000). *National Air Pollutant Emission Trends: 1900–1998*. United States Environmental Protection Agency, EPA Report No. EPA-454/R-00-002.

Nowack, B., and Bucheli, T. D. (2007). Occurrence, Behavior and Effects of Nanoparticles in the Environment, *Environ. Pollut.* 150:5–22.

Onischuk, A. A., di Stasio, S., Karasev, V. V., Strunin, V. P., Baklanov, A. M., and Panfilov, V. N. (2000). Evidence for Long-Range Coulomb Effects During Formation of Nanoparticle Agglomerates from Pyrolysis Combustion Routes, *J. Phys. Chem. A.* 104:10426–10434.

Pope, C. J., and Howard, J. B. (1997). Simultaneous Particle and Molecule Modeling (SPAMM): An Approach for Combining Sectional Aerosol Equations and Elementary Gas-Phase Reactions, *Aerosol Sci. Tech.* 27:73–94.

Pratsinis, S.E. (1998). Flame Aerosol Synthesis of Ceramic Powders, *Prog. Energy Combust. Sci.* 24:197–219.

Qin, Y., and Fichthorn, K. A. (2003). Molecular–Dynamics Simulation of Forces between Nanoparticles in a Lennard-Jones Liquid, *J. Chem. Phys.* 119:9745–9754.

Radzilowski, L. H., Carragher, B. O., and Stupp, S. I. (1997). Three-Dimensional Self-Assembly of Rodcoil Copolymer Nanostructures, *Macromolecules.* 30:2110–2119.

Reetz, M. T., Maase, M., Schilling, T., and Tesche, B. (2000). Computer Image Processing of Transmission Electron Micrograph Pictures as a Fast Reliable Tool to Analyze the Size of Nanoparticles, *J. Phys. Chem. B.* 104:8779–8781.

Sorensen, C. M. (2001). Light Scattering by Fractal Aggregates: A Review, *Aerosol Sci. Tech*. 35: 648–687.

Sinyagin, A., Belov, A., and Kotov, N. (2005). Monte Carlo Simulation of Linear Aggregate Formation from CdTe Nanoparticles, *Model. Sim. Mater. Sci. Eng.* 13:389–399.

Suh, S.-M., Zachariah, M. R., and Girshick, S. L. (2001). Modeling Particle Formation during Low-Pressure Silane Oxidation: Detailed Chemical Kinetics and Aerosol Dynamics, *J. Vac. Sci. Tech. A.* 19:940–951.

Tian, K., Liu, F., Yang, M., Thomson, K. A., Snelling, D. R., and Smallwood, G. J. (2007). Numerical Simulation Aided Relative Optical Density Analysis of TEM Images for Soot Morphology Determination, *Proc. Combust. Inst.* 31:861–868.

Tian, K., Thomson, K. A., Liu, F., Snelling, D. R., Smallwood, G. J., and Wang, D. (2006). Determination of the Morphology of Soot Aggregates using the Relative Optical Density Method for the Analysis of TEM Images, *Combust. Flame*. 144:782–791.

Ulrich, G. D. (1971). Theory of Particle Formation and Growth in Oxide Synthesis Flames, *Comb. Sci. Tech.* 4:47–57.

Ulrich, G. D., Milnes, B. A., and Subramanian, N. S. (1976). Particle Growth in Flames. 2. Experimental Results for Silica Particles, *Comb. Sci. Tech.* 14:243–249.

Wooldridge, M. S. (1998). Gas-Phase Combustion Synthesis of Particles, *Prog. Energy Combust. Sci.* 24:63–87.

Wooldridge, M. S., Torek, P. V., Donovan, M. T., Hall, D. L., Miller, T. A., Palmer, T. R., and Schrock, C. R. (2002). An Experimental Investigation of Gas-Phase Combustion Synthesis of SiO2 Nanoparticles using a Multi-Element Diffusion Flame Burner, *Combust. Flame*. 131:98–109.

Wu, J. J., and Flagan, R. C. (1988). Discrete-Sectional Solution to the Aerosol Dynamic Equations, *J. Colloid Interface Sci.* 123:339–352.

Wu, J. J., Nguyen, H. V., and Flagan, R. C. (1987). Method for the Synthesis of Submicron Particles, *Langmuir*. 3:266–271.

Xiong, Y., and Pratsinis, S. E. (1991). Gas Phase Production of Particles in Reactive Turbulent Flows, *J. Aerosol Sci.* 22:637–655.

Xiong, Y., and Pratsinis, S. E. (1993). Formation of Agglomerate Particles by Coagulation and Sintering. Part I. A Two-Dimensional Solution of the Population Balance Equation, *J. Aerosol Sci.* 24:283–300.

Yazicioglu, A. G., Megaridis, C. M., Campbell, A., Lee, K.-O., and Choi, M. Y. (2001). Measurement of Fractal Properties of Soot agglomerates in Laminar Coflow Diffusion Flames using Thermophoretic Sampling in Conjunction with Transmission Electron Microscopy and Image Processing, *Combust. Sci. Tech.* 171:71–87.

Zachariah, M. R., and Carrier, M. J. (1999). Molecular Dynamics Computation of Gas-Phase Nanoparticle Sintering: A Comparison with Phenomenological Models, *J. Aerosol Sci.* 30:1139–1151.

Zachariah, M. R., Carrier, M. J., and Blaisten-Barojas, E. (1994a). Atomistic Simulation of Vapor-Phase Nanoparticle Formation, in*Molecularly Designed Ultrafine/Nanostructured Materials*, K. E. Gonsalves, G.-M. Chow, T. D. Xiao, and R. C. Cammarata, eds., Materials Research Society, Pittsburgh, 343–348.

Zachariah, M. R., Carrier, M. J., and Blaisten-Barojas, E. (1994b). Molecular Dynamics Simulation of Large Cluster Growth, in *Gas Phase and Surface Chemistry*, T. J. Mountziaris, G. R. Paz-Pujalt, F. T. J. Smith, and P. R. Westmoreland, eds., Materials Research Society, Pittsburgh, 75–80.

Zachariah, M. R., and Semerjian, H. G. (1989). Simulation of Ceramic Particle Formation: Comparison with In-Situ Measurements, *AIChE Journal*. 35:2003–2012.

Zachariah, M. R., and Tsang, W. (1993). Application of Ab Initio Molecular Orbital and Reaction Rate Theories to Nucleation Kinetics, *Aerosol Sci. Tech.* 19:499–513.

Zachariah, M. R., and Tsang, W. (1994). Theoretical Prediction of Gas-Phase Nucleation Kinetics of SiO, in *Gas Phase and Surface Chemistry*, T. J. Mountziaris, G. R. Paz-Pujalt, F. T. J. Smith, and P. R. Westmoreland, eds., Materials Research Society, Pittsburgh, 19–24.